PHYSICAL REVIEW MATERIALS **8**, 084002 (2024)

Tuning the electronic structure of monolayer MoS_2 towards metal like via vanadium doping

Dipak Maity,[1] Rahul Sharma,[1,2,*] Krishna Rani Sahoo,[1] Ashique Lal,[1]
Raul Arenal,[3,4,5] and Tharangattu N. Narayanan[1,†]
[1] *Tata Institute of Fundamental Research Hyderabad, Sy. No. 36/P Serilingampally, Mandal 500046, India*
[2] *Department of Physics and Astronomy, Uppsala University, SE-751 20 Uppsala, Sweden*
[3] *Instituto de Nanociencia y Materiales de Aragon (INMA), CSIC-Universidad de Zaragoza, 50009 Zaragoza, Spain*
[4] *Laboratorio de Microscopias Avanzadas (LMA), Universidad de Zaragoza, 50018 Zaragoza, Spain*
[5] *Fundación ARAID, 50018 Zaragoza, Spain*

(Received 26 April 2024; revised 30 May 2024; accepted 15 July 2024; published 7 August 2024)

Doping of two-dimensional layered semiconducting materials is becoming pivotal in tailoring their electronic properties, enabling the development of advanced electronic and optoelectronic devices, where the selection of dopant is important. Here, we demonstrate the potential of substitutional vanadium (V) doping in monolayer molybdenum disulfide (MoS_2) lattice in different extents leading to tunable electronic and optoelectronic properties. We found that low-level V doping (~1 at. %) induces *p*-type characteristics in otherwise *n*-type monolayer MoS_2, whereas medium-level doping (~5 at. %) leads to an ambipolar semiconductor. Degenerately doped MoS_2 (~9 at. %) facilitates a transition from semiconducting towards metallic (metal-like) with reduced electrical resistivity (~4.5 Ω m of MoS_2 to $\sim 2.2 \times 10^{-5}$ Ω m), low activation energy for transport (~11 meV), and electric field independent drain current in field effect transistor–based transfer characteristics. A detailed temperature- and power-dependent photoluminescence study along with density functional theory–based calculations in support unravels the emergence of an excitonic transition at ~850 nm with its intensity dependent on the amount of vanadium. This study shows the potential of V doping in MoS_2 for generating multifunctional two-dimensional materials for next generation electronics, optoelectronics, and interconnects with systematic control over its electronic structure in a wide range.

DOI: 10.1103/PhysRevMaterials.8.084002

I. INTRODUCTION

In the realm of material sciences, electronic structure tunability plays a pivotal role, especially in enhancing the usability of materials across domains such as in optoelectronics, spintronics, catalysis, magnetism, etc. [1–5]. This aspect becomes crucial in the context of semiconducting two-dimensional (2D) materials, given the limited natural availability of semiconducting monolayer materials [4,6]. Monolayer molybdenum disulfide (MoS_2), an important 2D semiconducting transition metal dichalcogenide (TMD), has been extensively studied due to its direct optical band gap at visible energies (~1.9 eV), valley selective optical excitation possibilities due to high spin valley coupling, and high spin-orbit coupling (SOC) [7–9]. Researchers are delving into both chalcogen- and metal-based substitutional doping in the MoS_2 lattice for tuning its band gap, SOC, and magnetism [10–12]. While chalcogen-based doping to the level of alloying has been successfully implemented with dopants such as sulfur, selenium, and tellurium, metal-based high-level doping, which can significantly alter the band gap, remains limited to a few transition metals such as W, Re, Ni, and Nb [12–16]. Since the valence band maxima and conduction band minima in semiconducting TMDs typically have a higher contribution from *d* orbitals of transition metals, doping with these metals offers opportunities in tuning the electronic and optical properties [17–19].

Electronic transport studies indicate that MoS_2 grown via chemical vapor deposition (CVD) is an *n*-type material [20–22]. The presence of sulfur vacancy occurring during the CVD-based synthesis can be attributed to this *n*-type behavior of MoS_2, though this attribute is still in debate [23–25]. Substitutional doping with elements such as Nb, P, and W are proven to induce *p*-type electronic nature in MoS_2 [26,27]. Recently, vanadium (V) doping in TMDs is shown to bring interesting attributes such as valley polarization, tunable carrier density, dilute magnetism, etc. [13,28–30]. As an example, Williamson *et al.* demonstrated *p*-type semiconducting behavior due to 2% V doping in MoS_2 from electronic density of state (DOS) calculations [31]. Reports indicate that vanadium doping not only makes the *p*-doping nature in MoS_2, but also brings ferromagnetic ordering into the system [32,33]. In another study, Mao *et al.* reported that V doping promotes grain refinement and introduces numerous point defects along

---

[*] Contact author: rahuluppsala@gmail.com
[†] Contact author: tnn@tifrh.res.in

with p doping in MoS_2 powders [34]. Additionally, theoretical studies predict that V doping can also introduce spin polarization in MoS_2 band structure [19,35]. Although a few reports exist on the modification of the electrical properties of MoS_2 by V doping, a systematic study on the tunability of the electronic and optical properties of monolayer MoS_2 by V is still lacking.

Here we study both theoretically and experimentally the changes in the electronic and optical properties of monolayer MoS_2 (MS) with different amounts of V, where it is varied from ∼1 to ∼9 at. % coined as VMS-L (1%), VMS-M (5%), and VMS-H (9%). The substitutional doping of V in MS can be proposed to introduce a p-doping effect due to the differences in the oxidation states of Mo (4+) and V (5+), as proven here by the spectroscopic and transport studies.

VMS monolayers are synthesized using a CVD technique and have been characterized by scanning transmission electron microscopy (STEM) and x-ray photoelectron spectroscopy (XPS). The transport properties of V-doped MS are conducted to understand the p dopant effect of V atoms with varying concentration. The effects of doping on the work function and carrier density are also studied using transport measurements. The semiconductor to *metal-like* transition is observed with a high level of doping. A low-temperature photoluminescence (PL) study of the VMS reveals the formation of an excitonic state (V peak) at ∼850 nm with its dependence on the amount of V. A detailed temperature- and power-dependent PL study is conducted to understand the origin of this state. Experimental observations are further verified using density functional theory (DFT) –based first-principles calculations.

II. EXPERIMENTAL METHODS

A. MS and VMS Synthesis

VMS synthesis was carried out using a CVD-assisted method having a quartz tube of length ∼120 cm and inner diameter ∼5 cm. A schematic of the synthesis method is shown in the Supplemental Material, Fig. S1 [36]. In this method, MoO_3 (5 mg), vanadium oxide (V_2O_5) powders (5–15 mg), and sodium chloride (NaCl) were used as precursors, where they were kept in an alumina boat. The Si/SiO_2 (300 nm) substrate was kept on the top of the boat. Another alumina boat was used for sulfur (300 mg), and both these boats were placed inside the CVD quartz tube while keeping the sulfur boat at the left and the precursor boat at the right, as shown in Fig. S1 [36]. The distance between these two boats was kept as ∼15 cm. The growth temperature of the sulfur side was 210 °C and the temperature of the precursor side was 710 °C. The temperature ramp time to achieve 710 °C was kept as 25 min and the growth time was ∼15 min with a gas flow rate of ∼185 sccm (SCCM denotes cubic centimeter per minute at STP).

In order to ensure the absence of sulfur vacancies in MS and VMS grown via the above-mentioned process, further annealing of the samples with sulfur powder was also carried out. Sulfur annealing was carried out at 180 °C with a nitrogen flow rate of 100 sccm for 60 min.

B. Transmission electron microscopy measurements

High-resolution scanning transmission electron microscopy analyses were conducted in a probe-corrected Thermo Fisher Scientific Titan low-base microscope, operated at 120 keV, fitted with an X-FEG gun and Cs-probe corrector (CESCOR from CEOS GmbH) and a convergence angle of 25 mrad.

C. X-ray photoelectron spectroscopy (XPS)

XPS data was recorded on a Kratos Axis Supra spectrometer equipped with a monochromated Al $K\alpha$ x-ray source using an analyzer pass energy of 160 eV for survey spectra and 20 eV for the core-level spectra. Spectra were recorded by setting the instrument to the hybrid lens mode and the slot mode providing approximately a $700 \times 300\ \mu m^2$ analysis area using charge neutralization.

D. Low-temperature Raman and PL measurements

Low-temperature Raman and PL spectroscopic studies were carried out using a low-temperature liquid nitrogen setup (Linkham cell HSF-600). The Raman studies (using Renishaw inVia Raman spectrometer) were conducted using 532-nm laser excitation and PL studies using the Raman spectrometer are conducted with 633 nm excitation. The PL measurements were taken from room temperature to −196 °C, where the spectrum at each temperature of both heating and cooling were verified.

E. Transport measurements

Devices were fabricated using laser lithography. The metal deposition for the devices was done using a thermal evaporator. Finally, the devices were developed in acetone with mild sonication. All measurements were done in ambient environment with a Keithley 2450 source meter.

F. DFT studies

First-principles DFT–based calculations were carried out using the QUANTUM ESPRESSO 6.8 package with a plane-wave basis set (50-Ry cutoff) and norm-conserving pseudopotentials. The exchange-correlation energy of electrons was approximated with a local density approximation and a parametrized functional of Perdew and Zunger. A vacuum of ∼20 Å was added, separating adjacent periodic images along the z direction. The lattice parameter of a monolayer MoS_2 unit cell was optimized to 3.1667 Å using Brillouin zone sampling of $12 \times 12 \times 1$. Further, lattice vibrational modes of the unit cell were calculated using uniform grids ($nq1$, $nq2$, $q3$), where $n = 4$. Further structures of MoS_2 were simulated using a 6×6 periodic supercell with different levels of V doping and S vacancies, where integrations over the Brillouin zone were sampled with uniform 2×2×1.

III. RESULTS AND DISCUSSION

Monolayer VMS and MS were grown using a home-built CVD technique, as explained in the Experimental section and the Supplemental Material, Figs. S1(a) and S1(b) [36]. V_2O_5

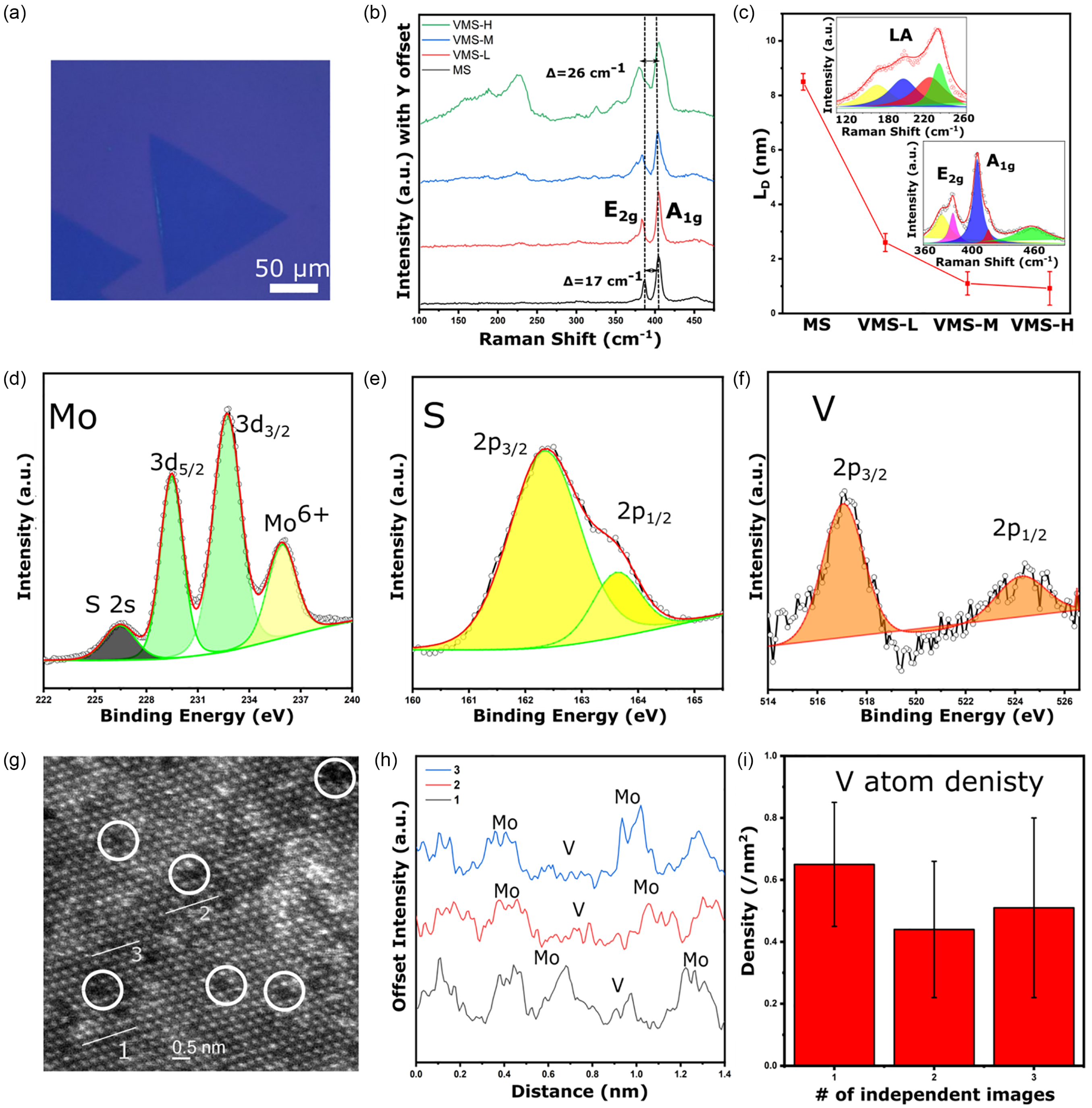

FIG. 1. (a) Optical image of a monolayer VMS. VMS crystals of more than 100 μm width are shown to be formed. (b) Raman spectra of MS and VMS having three different levels of V contents. (c) Average distance between defect size (L_D) analyzed using Raman studies of samples as a function of different levels of V content. High-resolution XPS spectra for VMS-M for (d) Mo, (e) S, and (f) V. (g) STEM-HAADF image of VMS-M monolayer showing the presence of V dopants. (h) Line profiles extracted from the STEM image of Fig. 1(g); see highlighted lines in the micrograph. (i) V atom density in three independent STEM-HAADF images. The density is calculated in 10 × 10 nm^2 areas to average it out.

and NaCl powders were added with the MoO_3 powder precursor for the V-doping process. The MoO_3-V_2O_5 ratios were set to be 1:1, 1:2, and 1:3 for achieving three different doping concentrations of V in VMS, namely, VMS-L, VMS-M, and VMS-H, respectively. Figure 1(a) shows the optical image of VMS-L showing a triangular monolayer crystal similar to pristine MS of similar size. A photograph of MS is given in the Supplemental Material, Fig. S1(c) [36]. The different extent of V doping in VMS does not have much effect on the morphology of the crystals. It is important to mention that, by optimizing the growth parameters we may be able to synthesize monolayer V-doped MoS_2 samples in the form of a single crystal as well as large area films as shown in Supplemental Material Fig. S10 [36]. The maximum lateral width of the single crystal obtained is ∼150 μm [Fig. S10(a) [36]] and the dimension of the large area uniform film is ∼500 μm ×300 μm [Fig. S10(b) [36]].

Figure 1(b) shows the micro-Raman spectra of VMS and MS. MS shows two typical vibration modes, namely, E_{2g} [in-plane vibration, sum of degenerate transverse optical (TO) and longitudinal optical (LO) branch] and A_{1g} [out-of-plane vibration, out-of-plane optical (ZO)] modes at 384 and 401 cm^{-1}, respectively [10,37,38]. A separation of ∼17 cm^{-1} among E_{2g} and A_{1g} modes confirms the presence of monolayer MS [37,38]. In the case of VMS, the separation between E_{2g} and A_{1g} peaks enhances from 17 to 26 cm^{-1} depending on the doping concentration. This enhancement resembles the phonon dispersion of vibration modes away from the gamma point ($q = 0$): ZO mode in an upward direction and LO and TO modes in a downward direction (see phonon dispersion of MoS_2 in Supplemental Material Fig. S2 [36]) [37]. The E_{2g} and A_{1g} peaks also become broader with increasing doping concentrations. The enhanced full width at half maximum (FWHM) of both E_{2g} and A_{1g} of VMS with doping is clearly seen in Fig. S3 (the FWHM of E_{2g} and A_{1g} changed from 4 and 6 cm^{-1} to ∼10 and ∼12 cm^{-1}) [36]. The broadness of the peaks may represent the presence of localized phonon modes [10]. Other than this broadening, a set of new peaks starts emerging in the range 100–260 cm^{-1}. These peaks are reported earlier for defect site-related peaks [37]. These peaks are attributed to a local maximum in the vibrational density of states, corresponding to the longitudinal acoustic (LA) branch at the edge of the Brillouin zone [37]. Phonon dispersion calculations for VMS reported by Zhang *et al.* reveal new complex lattice vibrations for V-doped MoS_2 compared to that of pristine MoS_2, indicating that the substitutional V dopants reduce the lattice symmetry [39]. The reduction in lattice symmetry and the presence of V dopants, which act as disorders in pristine MoS_2, are associated with the appearance of new Raman peaks.

The vanadium-doped sites are also acting as defects for the MoS_2 lattice, thus causing these peaks to emerge. To understand them better, Raman signatures of both the regions are deconvoluted: these regions are 100–260 cm^{-1} and 350–420 cm^{-1} [see inset of Fig. 1(c)]. The peaks in the proximity of first-order E_{2g} (at 377 cm^{-1}) and A_{1g} (at 411 cm^{-1}) Raman modes are LO and ZO branches at the M point, respectively [37]. While the four peaks fitted in the 100–260 cm^{-1} region are TA (transverse acoustic; 157 cm^{-1}) at M, ZA (out of plane acoustic; 187 cm^{-1}) at M, TA (215 cm^{-1}) at K, and LA (227 cm^{-1}) at M modes (see phonon dispersion of MoS_2 in Supplemental Material Fig. S2 [36]) [37]. The LA mode can particularly be used to calculate the average distance (L_D) between defect sites in MoS_2 (which is V atoms in our case) with the relation [37]

$$L_D^2 = \frac{I(A_{1g})}{I(\mathrm{LA})} C(A_{1g}), \tag{1}$$

where $I(A_{1g})$ and $I(\mathrm{LA})$ are the intensity of the A_{1g} mode and the LA(M) mode. $C(A_{1g})$ is the proportionality constant, which is 0.59 nm^2 for the A_{1g} mode [37]. The L_D values are calculated as ∼8.7, ∼2.6, ∼1.1, and ∼0.9 nm for MS, VMS-L, VMS-M, and VMS-H, respectively [see Fig. 1(c)]. From the calculated values of L_D, the density of V atoms can be calculated as $\sim 1 \times 10^{13}$ $\mathrm{atoms/cm}^2$, $\sim 8 \times 10^{13}$ $\mathrm{atoms/cm}^2$, and $\sim 15 \times 10^{13}$ $\mathrm{atoms/cm}^2$, respectively, for VMS-L, VMS-M, and VMS-H (see Supplemental Material [36]). This gives the estimated value of V doping to be ∼1%, ∼5%, and ∼9% for VMS-L, VMS-M, and VMS-H, respectively. The dopant amount (in VMS-M) is further confirmed from STEM and x-ray photoelectron spectroscopy (XPS) –based analyses (Supplemental Material Figure S4 [36]).

The effect of V doping on the chemical bonding of MoS_2 is further understood by comparing the XPS of MS with VMS. The survey spectrum of VMS-M shows the presence of V, Mo, and S in VMS, as shown in Fig. S4 [36]. Figure 1(c) shows the high-resolution XPS spectra of Mo $3d$, S $2p$, and V $2p$. A Mo doublet is observed at ∼229.4 eV ($3d_{5/2}$) and ∼232.7 eV ($3d_{3/2}$) [Fig. 1(d)] [10,12]. Apart from this, a small Mo^{6+} peak is also observed at ∼235.9 eV indicating the presence of some MoO_3 particles (ingrown nucleation sites) in the sample [12,40]. The positions of the S $2p$ doublets are at 162.3 ($2p_{3/2}$) and 163.6 ($2p_{1/2}$) eV [Fig. 1(e)] [10]. The V $2p$ peak is also observed in the XPS. The $2p$ doublets of V are at ∼517.2 eV ($2p_{3/2}$) and ∼524.3 eV ($2p_{1/2}$) [Fig. 1(f)] [29]. The peak positions of Mo and S are observed to be shifted towards lower binding energies (see Fig. S4 [36]). This shows that the V doping is lowering the Fermi level of MS towards the valence band causing p doping in MS [29].

V doping is further confirmed using STEM-high angle annular dark field (STEM-HAADF) imaging of VSM-M. Figure 1(g) displays the atomic resolution image of VMS showing the lower intensity points in Mo atomic columns. These lower intensity points are reported to be the presence of V atoms in the MS lattice [11–13]. The distribution of V is found to be random and does not favor clustering [13]. Figure 1(h) shows the line profiles corresponding to three different locations in Fig. 1(h). A clear and sudden decrease in the intensity at certain locations confirms the presence of lower atomic number V atoms as the atomic intensities in STEM are dependent on the atomic number variations [13]. The number density of V is calculated manually using three different independent STEM images [see Fig. 1(i)]. The value ∼0.5 $\mathrm{atom/nm}^2$ corresponding to ∼4 at. % doping of V, matches well with the XPS and Raman analyses.

A. Electronic transport studies

It has been found from the XPS studies, discussed previously, that V doping can reduce the Fermi level of MS towards the valence band [13,29]. To examine the effect of doping in electronic transport, electric field controlled transport studies are conducted using a top gated field effect transistor development. Figure 2(a) shows the schematic of a device used for the transport measurements of MS, VMS-L, VMS-M, and VMS-H. Figure 2(b) shows the four-probe current-voltage (I-V) characteristics of MS and VMS-L/M/H. The I_{ds} current for MS is in the nanoampere range with a drain source voltage range of −1 to +1 V at 0 V V_{gs} (gate-source voltage). While in the case of VMS, I_{ds} values are found to be in the order of $\sim 10^{-8}$, 10^{-5}, and 10^{-4} A for VMS-L, VMS-M, and VMS-H, respectively. These very different I_{ds} current ranges can be understood by investigating the Ioffe-Regel criterion [41]. This criterion indicates that $k_F l_e \gg 1$ for metals and $k_F l_e \ll 1$

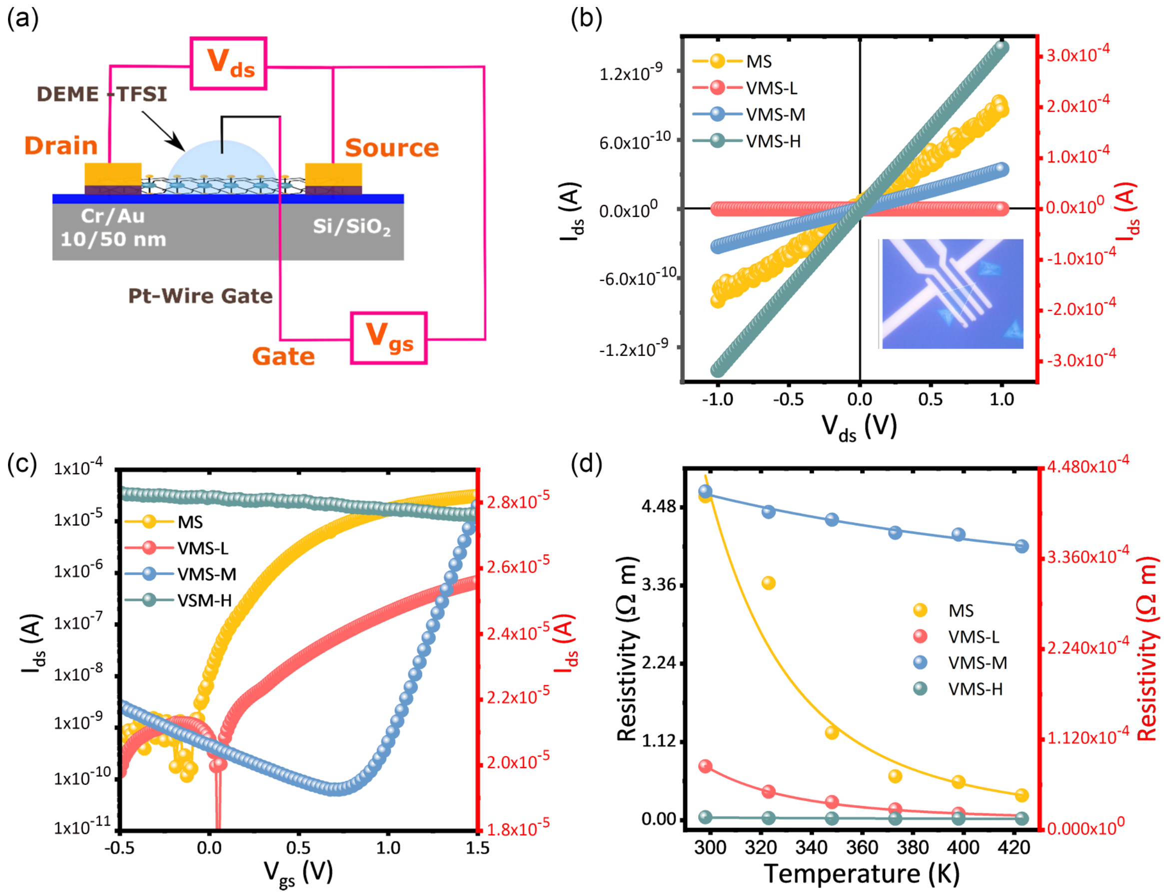

FIG. 2. (a) Schematic of MS/VMS-based field effect transistor (FET) with DEME-TFSI ionic liquid as (top) gating dielectric material. (b) Room temperature four-probe current-voltage (I-V) characteristics curves of MS as well as VMS of three different V concentrations. The y axis (current) for MS (left side with black color) and VMS-L/M/H (right side with red color) are shown in the same figure. (c) Top gated FET characteristics: I_{ds} vs V_{gs} curves of MS and VMS at $V_{ds} = 0.5$ V. VMS-H is multiplied by 0.5 to put in the same graph for comparison. The y axis (current) is in logarithmic scale for MS and VMS-L on the left side with black color and for VMS-M/H on the right side with red color, respectively. (d) Resistivity vs temperature curve for MS and VMS. The y axis (current) for MS and VMS-L are on the left side with black color and that for VMS-M/H is on the right side with red color, respectively.

for insulator, where $k_F(=\sqrt{2\pi n_{2\mathrm{D}}})$ is the Fermi wave vector with $n_{2\mathrm{D}}$ as the carrier density [41]. The $l_e(=\frac{hk_F\sigma}{2\pi n_{2\mathrm{D}}e^2})$ is the mean free path of electrons with σ as the conductivity. For the four-probe based device analyses at $V_{\mathrm{gs}} = 0$ V, MS has $k_F l_e \sim 10^{-1}$, indicating their insulating nature. The values of $\sim 10^4$ are obtained for VMS-H, indicating metallic nature compared to MS. This confirms that high V doping can cause an insulator to metal-like transition in MS.

The ionic liquid Diethylmethyl(2-methoxyethyl) ammonium bis(trifluoromethylsulfonyl) imide (DEME-TFSI), assisted gating voltage is applied to study the electron transfer characteristics. The transfer characteristics of MS, VMS-L, VMS-M, and VMS-H are shown in Fig. 2(c). The MS device shows a typical n-type behavior in the I_{ds} vs V_{gs} graph with a threshold voltage (V_{th}) at ~ -0.1 V. On the other hand, VMS-L showed that the V_{th} is at ~ 0.06 V. The VMS-M shows ambipolar behavior with V_{th} at 0.8 V. The VMS-H being metallic shows an almost independent nature in the current variation with the gating voltage. The positive shift of V_{th} in VMS-L and VMS-M with respect to MS indicate the p-type doping [42,43]. The carrier concentration, $n_{2\mathrm{D}}$, for MS, VMS-L, and VMS-M can be calculated using a parallel plate capacitor model by formula [41,43]

$$n_{2\mathrm{D}} = \frac{C_{\mathrm{ox}}\Delta V_{\mathrm{gs}}}{e}, \tag{2}$$

where C_{ox} is the parallel plate capacitance of dielectric, $\Delta V_{\mathrm{gs}} = V_{\mathrm{gs}} - V_{\mathrm{th}}$ (V_{gs} is any voltage in On state), and e is the elementary charge, $1.602 \times 10^{-19} C$. At $V_{\mathrm{gs}} = 1.5$ V, $n_{2\mathrm{D}}$ of electrons is calculated as $\sim 7 \times 10^{13}$, $\sim 6 \times 10^{13}$, and $\sim 3 \times 10^{13}$ cm^{-2} for MS, VMS-L, and VMS-M, respectively (details are given in the Supplemental Material [36]).

This significant and constant decrease in electron density with V doping clearly shows that the V atoms are acting as intrinsic p dopants for MS.

The effect of V doping on the work function of MS can be seen by calculating it using a formula for change in work function ($\Delta\Phi$) [43]:

$$\Delta\Phi = \Phi_{\mathrm{VMS}} - \Phi_{\mathrm{MS}} = \ln\left(\frac{n_{2\mathrm{D,MS}}}{n_{2\mathrm{D,VMs}}}\right), \tag{3}$$

where Φ_{VMS} and Φ_{MS} are the work functions of VMS and MS, respectively. $n_{2\mathrm{D}}$ is the carrier density extracted from the FET measurements. The calculated $\Delta\Phi$ for VMS-L and VMS-M is ~105 and ~826 meV, respectively (detailed calculation given in the Supplemental Material [36]). This positive lift in Fermi level indicates that the *p*-doping behavior of V doping. This observation matches well with the DFT–based calculated values where the $\Delta\Phi$ is calculated as ~720 meV for ~4 at. % V doping.

The slope of the linear region of the transfer curve was then used to calculate the mobility of electrons and holes with the formula [41,44]

$$\mu_{e,h} = \frac{L}{WV_{\mathrm{ds}}C}\left(\frac{dI_{\mathrm{ds}}}{dV_{\mathrm{gs}}}\right)_{e,h}, \tag{4}$$

where μ is the mobility for an electron or hole and L and W are the length and width of the channel device, respectively. C is the gate capacitance per unit area (7.2 μF cm^{-2}) and $(\frac{dI_{\mathrm{ds}}}{dV_{\mathrm{gs}}})$ is the slope of the transfer curve [41,45]. The μ_e for MS is calculated as ~7.8 cm^2 V^{-1} s^{-1}. In the case of VMS-M, μ_e and μ_h are found to be 26 cm^2 V^{-1} s^{-1} and 17 cm^2 V^{-1} s^{-1}, respectively.

The semiconductor to metal-like transition is further confirmed with temperature-dependent resistivity measured for MS and VMS L/M/H in the high-temperature range (300–473 K), as shown in Fig. 2(d). MS and VMS L/M are found to have thermally activated transport as the resistivity decreases with an increase in temperature while the VMS-H shows negligible change in its resistivity for the temperature range 300–473 K. Thus, the temperature dependence of resistivity of MS, VMS-L/M was fitted with the Arrhenius equation [41]

$$\rho = \rho_o e^{E_a/K_bT}, \tag{5}$$

where ρ is the resistivity, K_b is the Boltzmann constant, and E_a is the activation energy for thermally activated transport. The E_a is ~ 214, ~ 196, ~ 21, and ~ 11 meV for MS, VMS-L, VMS-M, and VMS-H, respectively. Notably, the activation energies for VMS-M and VSM-H are less than the room temperature energy (~25.7 meV) which makes them highly conductive at room temperature.

The transport measurements show that the V doping not only tunes the electrical properties of MS but at the same time it can change its behavior from an *n*-type semiconductor to ambipolar to metallic-like at the degenerate doping levels of 9%.

B. Photoluminescence and new excitonic state

The PL spectra from VMS L/M/H doping percentages are compared in Supplemental Material Fig. S5 [36]. The higher V doping significantly reduces the PL intensity due to its metal-like behavior. Here, we are comparing the power and temperature PL spectra from MS and VMS-M in detail for a better understanding of the effect of V doping. Detailed temperature-dependent (−196 °C to 30 °C) PL measurements are conducted for MS and VMS-M samples, as shown in Supplemental Material Fig. S6 [36]. The A^- trion contribution is found to be significantly reduced in the deconvoluted PL spectrum of VMS-M while comparing with that of MS (see Fig. S7 [36]).

Figures 3(a) and 3(b) are showing the PL spectra at −196 °C for pristine MS and VMS-M samples. The MS PL shows two well-known A and B excitonic peaks arising from the valence band splitting due to high spin-orbit coupling in MS [10,46,47]. A new peak can also be observed at ~720 nm which can be considered a defect peak [46]. The most common types of defects that can be observed in an as-grown MS are single chalcogen vacancies (S_v), double chalcogen vacancies (S_{2v}), and metal vacancies (M_v) [48]. The formation energies of these respective defects are calculated in our previous work [10]. The formation energy of M_v is ~5 eV while that for S_v and S_{2v} are ~2 and ~3 eV, respectively [10].

Thus, M_v is rare to be observed in the low-temperature PL of MS [46]. Earlier low-temperature PL reports have already shown sulfur vacancy-related PL at ~720 nm in MS [10,46]. The fact that we observe a new peak at low temperatures may be related to adsorbed molecules, or to chalcogen vacancies [49,50]. Thus, the peak at ~720 nm can be attributed to sulfur vacancy defects bound excitonic emission and is named as $\mathrm{Ex}_{\mathrm{S\,vac}}$ in the upcoming discussion. The low-temperature PL of VMS-M not only shows A exciton, B exciton, and $\mathrm{Ex}_{\mathrm{S\,vac}}$, but also shows an extra emission peak at ~850 nm. This new peak is observed in all the low-doped, medium-doped, and high-doped VMS (see Supplemental Material Fig. S5 [36]) but not in pristine MS. We called this new emission peak as Ex_{V} in the upcoming discussion. The evolutions of $\mathrm{Ex}_{\mathrm{S\,vac}}$ and Ex_{V} with temperature are shown in Fig. S6 [36]. Both $\mathrm{Ex}_{\mathrm{S\,vac}}$ and Ex_{V} peaks originate at lower temperatures, due to low binding energies. The $\mathrm{Ex}_{\mathrm{S\,vac}}$ starts to appear at ~−80 °C while the Ex_{V} starts to appear at ~−40 °C as shown in Fig. S6 [36].

The power-dependent PL for VMS is carried out where Ex_{V} increases monotonically with laser power as shown in Fig. 3(c). To understand its behavior better, the relative integrated PL (RIPL) contribution of each peak is plotted with respect to the power in Fig. 3(d). The contribution of RIPL from the A and B excitonic peaks increases continuously with laser power while for $\mathrm{Ex}_{\mathrm{S\,vac}}$ and Ex_{V}, it decreases as the laser power increases [see Fig. 3(c)]. The behaviors of the $\mathrm{Ex}_{\mathrm{S\,vac}}$ and Ex_{V} are observed to be the same with power. As the defect sites are constant in number and would not increase with laser power in the given power range, the RIPL is expected to decrease due to Pauli blocking [46]. In the case of VMS-M, the extra states may arise in the band gap of MS due to V doping, a fact later verified with DFT–based analyses. These states are also constant in number in a crystal and depend only on the doping concentration of V, thus showing a decrease in RIPL of the V peak as the states get filled easily with power as observed in Fig. 3(d).

This claim is further confirmed with the power-dependent PL measurements of Ex_{V} for low-, medium-, and high-doped VMS. In MS, the PL intensity increases linearly for the A and B excitonic peaks as shown in Fig. S7 [36] because of the availability of empty states in the conduction band. However, in the case of VMS, states belonging to Ex_{V} are expected to be proportional to the V concentration. Thus, the V peak intensity is sublinear with respect to power [Fig. 3(e)]. The proportionality constants are found to be ~0.31, 0.51, and 0.65 for low-, medium-, and high-doped VMS, respectively. This clearly indicates that the midgap states increase with the increase in V concentration. Secondly, the increase in V doping decreases the overall PL intensity as shown in Fig. S5 [36].

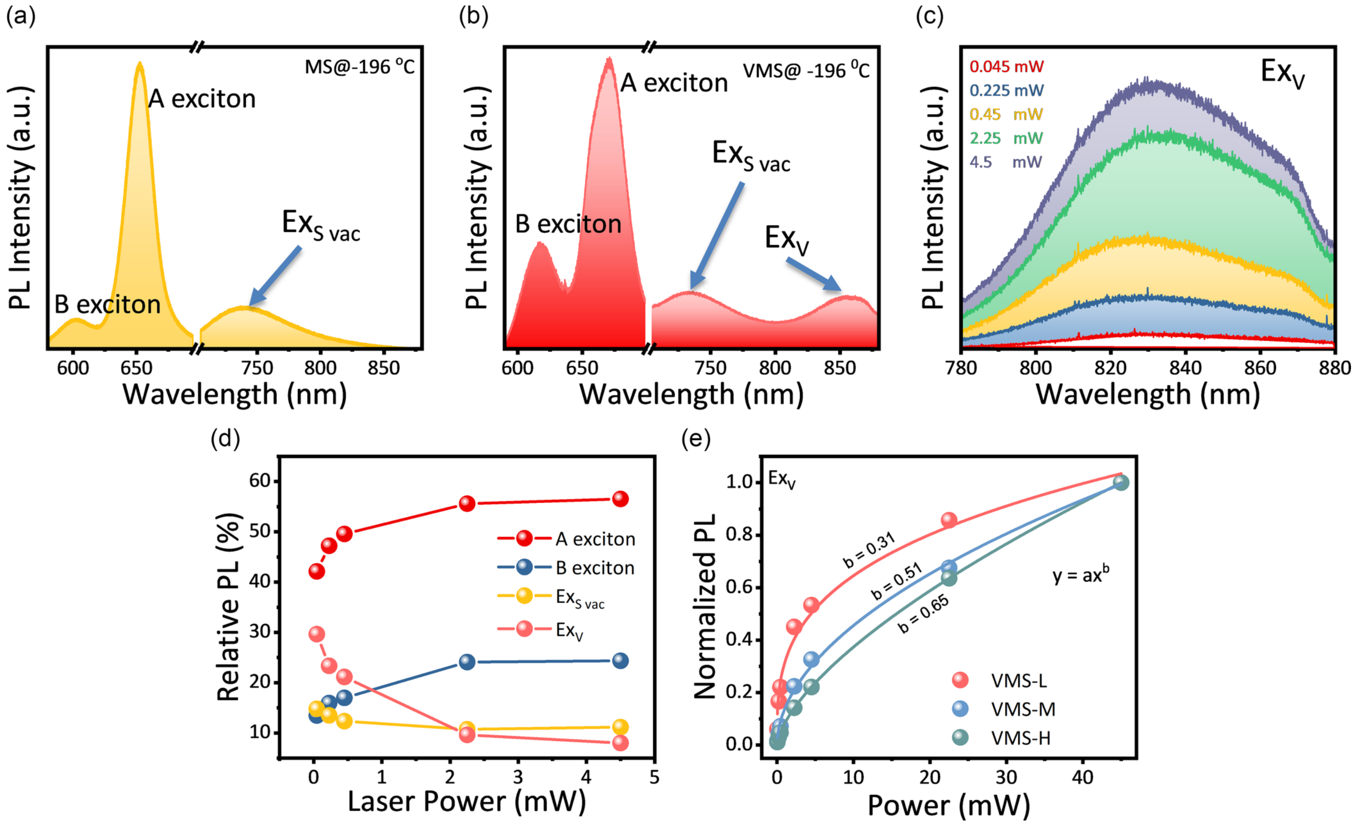

FIG. 3. Photoluminescence at $-196\,^\circ$C from (a) MS and (b) VMS-M with 532 nm excitation. (c) Power-dependent PL measurement of VMS-M. (d) Laser power vs relative PL (%) plot of VMS-M. (e) Normalized PL vs power plot of the V peak for three different doping concentrations.

To further confirm that the origin of the $\mathrm{Ex_V}$ is different from single chalcogen vacancy (S_v) or double chalcogen vacancy (S_{2v}), sulfur annealing is carried out in both MS and VMS at $200\,^\circ$C for 1 h and the PL spectra after annealing are shown in Fig. 4. All the graphs in Fig. 4 are normalized with respect to their *A* exciton peak. In the case of MS, the S peak decreases significantly after sulfur annealing, as shown in Figs. 4(a) and 4(b) [51]. The passivation of S vacancies with sulfur annealing can be the reason for the decrease in $\mathrm{Ex_{S\,vac}}$ excitonic emission in MS. In the case of VMS, the S annealing decreases the $\mathrm{Ex_{S\,vac}}$ as the S vacancies decrease [51] but the $\mathrm{Ex_V}$ intensity remains the same as shown in Figs. 4(c) and 4(d). This confirms that the origin of the $\mathrm{Ex_V}$ is different from the $\mathrm{Ex_{S\,vac}}$ and is coming from the V doping only.

A DFT–based study on the stabilized $6 \times 6 \times 1$ supercell of MS, MS lattice with a S vacancy (SMS), V-doped MS ($\sim$8.3% atomic doping with four atoms were replaced with V out of 36 Mo atoms) (VMS), and 8.3% V-doped MS with a S vacancy (SVMS) is carried out (details of the DFT study are given in the Experimental section and the Supplemental Material). The respective unit cells can be seen in Fig. S8 [36]. MS shows a direct band gap of $\sim$1.85 eV [Fig. 5(a)] at the high symmetry *K* point in momentum space, which is in tune with the experimental PL values observed here and also with the literature [52,53]. In SMS, the band gap remains the same but new extra states (deep levels) are emerging in the band gap [Fig. 5(b)] [54]. These states are arising due to the S vacancy in the system [10,54]. The states, working as acceptor levels, are closer to the conduction band and can be the reason for S peak in the low-temperature PL [10]. The VMS structure has three V atoms in the MS lattice. All the V atoms are placed close to each other to minimize the formation energy of the system. The band structure of VMS in Fig. 5(c) also shows some midgap states in the band structure. The states are closer to the valence band [19]. These states might be working as acceptors and can be a reason for the V peak in the PL at lower energies than *A*-excitonic emissions. In the case of SVMS, the band structure has two types of midgap states as shown in Fig. 5(d).

The one closer to the conduction band is from the S vacancy while the other ones closer to the valence band are from the V atoms. The same is confirmed with partial density of state calculations, as shown in Fig. 5(e). The contribution in S vac states (near the conduction band) are majorly coming from the Mo atoms [see Fig. 5(e)]. In the absence of S atoms, the vacant *d* orbitals of Mo are contributing to the midgap states, while the V states (near the valence band) are majorly coming from the V atoms with small contributions from the Mo and S states. The presence of these two types of midgap states can be a very possible reason for two excitonic emission peaks, i.e., the S vacancy peak and the V peak in VMS L/M/H crystals at low temperatures. It is important to highlight that among various magnetic dopants, V is unique in its ability to maintain high PL of $\mathrm{MoS_2}$ even at substantial level (5%) doping percentages. This distinct characteristic arises because the doping levels introduced by V atoms are not in

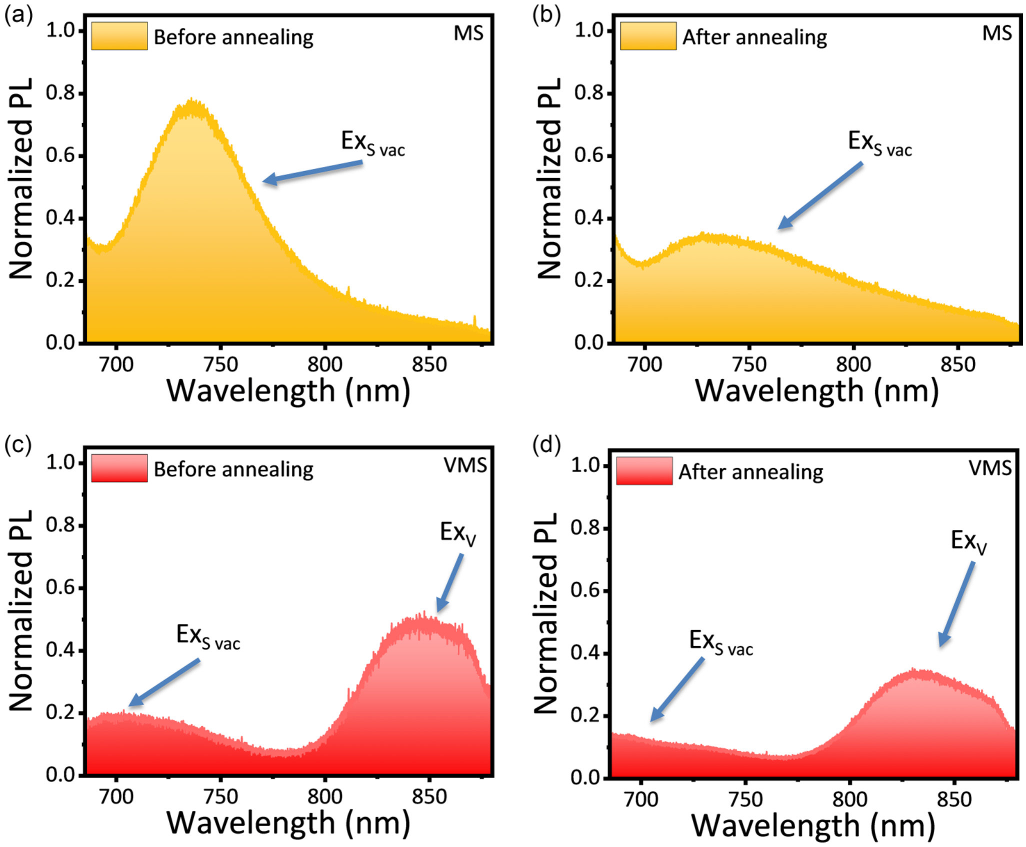

FIG. 4. Normalized PL measurement at −196 °C for (a) MS before annealing, (b) after annealing in sulfur environment, (c) VMS before annealing, and (d) VMS after annealing in an excess sulfur environment. All figures are normalized with respect to their *A* exciton and shown in the same wavelength range for clarity.

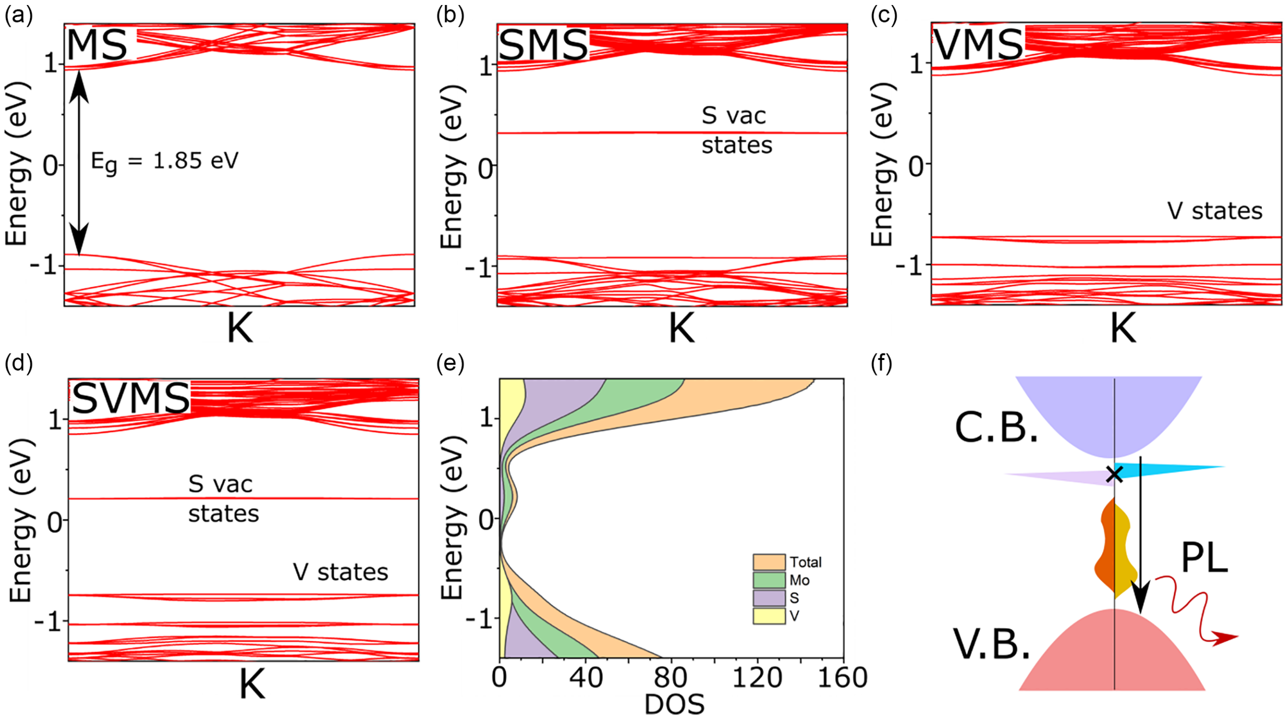

FIG. 5. Energy band (E-k) diagram plot using DFT for (a) MS, (b) MS lattice with a S vacancy (SMS), (c) V-doped MS (VMS), and (d) V-doped MS with a S vacancy(SVMS). (e) Partial density of state for SVMS showing orbital contributions from different atoms. (f) Schematic of VMS band structure which does not have dense states near the conduction band and hence favors the radiative recombination of photoexcited electrons.

close proximity to the conduction band edge, a phenomenon commonly observed with other dopants such as iron (Fe) and chromium (Cr) as shown by us through DFT in Fig. S9 [36]. Consequently, investigating V doping is crucial, as it offers significant valley polarization and spin splitting while preserving the PL intensity, as depicted in the schematic shown in Fig. 5(f). The sketch in Fig. 5(f) illustrates the VMS band structure, which lacks sharp density of states near the conduction band, thereby promoting the radiative recombination of photoexcited electrons. Detailed studies by Duan *et al.* suggest that the existence of a sharp density of states near the conduction band decreases photoluminescence [42]. A high state density provides a nonradiative deexcitation channel for excited conduction band photoelectrons [55]. Thus, the impurity band acts as a nonradiative recombination center, reducing the PL intensity. Other magnetic impurities like Fe and Co reduce the PL of MoS_2 because they have a sharp DOS near the conduction band (Fig. S9 [36]). In contrast, the V-doped MoS_2 system, with a low DOS near the conduction band, facilitates emission in the PL spectrum. Therefore, V doping is beneficial for achieving the coexistence of magnetism and photoluminescence. These attributes position the V doping as a unique area for study towards the development of next generation opto-spintronic devices—an area which demands further studies and explorations.

IV. CONCLUSION

Systematic tunability in the electronic properties of layered 2D materials is highly important in developing materials for next generation electronics and interconnects and here we show such a tunability with vanadium substitutional doping in monolayer MoS_2. Controllable doping of V in monolayer MS is demonstrated leading to the formation of low- (1%), medium- (5%), and high- (9%) level doped VMS monolayer crystals of large size (∼100 μm). Tunable electronic properties are demonstrated with controlled V doping where a semiconducting to metal-like transition is shown with low (1%) to high (9%) atomic percntage V doping. A systematic control over the *n*-type electronic transport nature of MS is shown to be achieved with vanadium doping where it is turned to a *p*-type semiconductor (with 1% doping) to ambipolar with medium-level doping (5%) to field-independent metal-like VMS monolayers at 9% V doping. The thermal activation barriers for the electronic transport in MS and doped VMS layers are seen to be systematically changed from a high value (∼214 meV for MS) towards below room temperature (∼11 meV for VMS-H) indicating a possible metal-like transition of MS with electric field independent drain-source current with low resistivity at degenerate doping levels of vanadium. Vanadium doping further brings new excitonic states in MS, as confirmed by the photoluminescence study. The emission intensity of this exciton is found to greatly depend on the amount of vanadium. Systematic variation in the electronic structure with V doping is also verified using DFT–based calculations and the emergence of midgap states in MS with V content is verified, indicating the consistency with the experimental observation. In a nutshell, this study promises the potential of vanadium doping, one of the highly reliable dopants for systematically tuning the electronic structure, in developing next generation 2D electronic materials for diverse applications.

ACKNOWLEDGMENTS

The authors from TIFR acknowledge the support of the Department of Atomic Energy, Government of India, under Project Identification No. RTI 4007. T.N.N. acknowledges the financial support from DST-SERB, Government of India SUPRA scheme (SPR/2020/000220). R.S. acknowledges Dr. Sumit Bawari for the discussion regarding DFT calculations. The TEM and XPS studies were performed in the Laboratorio de MicroscopiasAvanzadas (LMA), Universidad de Zaragoza (Spain). We thank G. Antorrena (LMA) for the XPS measurements. R.A. acknowledges support from Spanish MCIN (PID2019-104739GB-100/AEI/10.13039/501100011033), Government of Aragon [projects DGA E13-23R (FEDER, EU)] and from the European Union H2020 program Graphene Flagship (881603).

The authors declare no competing interests.

---

[1] R. Sharma, P. Sharma, K. R. Sahoo, S. Sankar, V. P. S. Awana, M. Kumar, and T. N. Narayanan, Giant photoresponsivity of transfer free grown fluorographene—MoS_2 heterostructured ultra-stable transistors, Mater. Today **50**, 69 (2021).

[2] D. Maity, M. Sahoo, K. R. Sahoo, S. K. Nayak, T. N. Narayanan, and R. Sharma, Strain-tunable ultrastable MoS_2/fluorographene hybrid photodetectors of high responsivity, ACS Appl. Electron. Mater. **5**, 5129 (2023).

[3] K. R. Sahoo, A. Guha, S. Bawari, R. Sharma, D. Maity, and T. N. Narayanan, Basal plane activation of MoS_2 by the substitutional doping of vanadium toward electrocatalytic hydrogen generation, ACS Appl. Energy Mater. **5**, 11263 (2022).

[4] E. C. Ahn, 2D materials for spintronic devices, npj 2D Mater. Appl. **4**, 17 (2020).

[5] B. Upadhyay, R. Sharma, D. Maity, T. N. Narayanan, and S. K. Pal, Ultrafast carrier dynamics in vanadium doped MoS_2 alloys, Nanoscale **15**, 16344 (2023).

[6] T. Wang, M. Park, Q. Yu, J. Zhang, and Y. Yang, Stability and synthesis of 2D metals and alloys: A review, Mater. Today Adv. **8**, 100092 (2020).

[7] D. Xiao, G. Bin Liu, W. Feng, X. Xu, and W. Yao, Coupled spin and valley physics in monolayers of MoS_2 and other group-VI dichalcogenides, Phys. Rev. Lett. **108**, 196802 (2012).

[8] W. F. Li, C. Fang, and M. A. Van Huis, Strong spin-orbit splitting and magnetism of point defect states in monolayer WS_2, Phys. Rev. B **94**, 195425 (2016).

[9] D. Maity, B. Upadhyay, J. J. Panda, K. R. Sahoo, A. Sreekant, G. Rajalakshmi, S. K. Pal, and T. N. Narayanan, Tuning the valley depolarization dynamics in selenium and vanadium alloyed monolayer MoS_2, Phys. Rev. Mater. **8**, 064004 (2024).

[10] R. Sharma, J. Pandey, K. R. Sahoo, K. S. Rana, R. K. Biroju, W. Theis, A. Soni, and T. N. Narayanan, Spectroscopic correlation of chalcogen defects in atomically thin $MoS_{(1-x)}Se_{2x}$ alloys, J. Phys. Mater. **3**, 045001 (2020).

[11] M. Pelaez-Fernandez, Y. C. Lin, K. Suenaga, and R. Arenal, Optoelectronic properties of atomically thin $Mo_xW_{(1-x)}S_2$ nanoflakes probed by spatially-resolved monochromated eels, Nanomaterials **11**, 3218 (2021).

[12] D. Maity, R. Sharma, K. R. Sahoo, J. J. Panda, A. Lal, A. B. Puthirath, P. M. Ajayan, and T. N. Narayanan, On the electronic and spin-valley coupling of vanadium doped $MoS_{2(1-x)}Se_{2x}$ Monolayers, J. Phys.: Condens. Matter **35**, 505002 (2023).

[13] S. Li, Tunable doping of rhenium and vanadium into transition metal dichalcogenides for two-dimensional electronics, Adv. Sci. **8**, 2004438 (2021).

[14] Q. Li, Enhanced valley Zeeman splitting in Fe-doped monolayer MoS_2, ACS Nano **14**, 4636 (2020).

[15] D. Mosconi, P. Till, L. Calvillo, T. Kosmala, D. Garoli, D. Debellis, A. Martucci, S. Agnoli, and G. Granozzi, Effect of Ni doping on the MoS_2 structure and its hydrogen evolution activity in acid and alkaline electrolytes, Surfaces **2**, 531 (2019).

[16] M. B. Sreedhara, Y. Miroshnikov, K. Zheng, L. Houben, S. Hettler, R. Arenal, I. Pinkas, S. S. Sinha, I. E. Castelli, and R. Tenne, Nanotubes from ternary $WS_{2(1-x)}Se_{2x}$ alloys: Stoichiometry modulated tunable optical properties, J. Am. Chem. Soc. **144**, 10530 (2022).

[17] M. Fang and E. H. Yang, Advances in two-dimensional magnetic semiconductors via substitutional doping of transition metal dichalcogenides, Materials (Basel). **16**, 3701 (2023).

[18] M. Koperski, M. R. Molas, A. Arora, K. Nogajewski, A. O. Slobodeniuk, C. Faugeras, and M. Potemski, Optical properties of atomically thin transition metal dichalcogenides: Observations and puzzles, Nanophotonics **6**, 1289 (2017).

[19] X. L. Fan, Y. R. An, and W. J. Guo, Ferromagnetism in transitional metal-doped MoS_2 monolayer, Nanoscale Res. Lett. **11**, 154 (2016).

[20] H. Schmidt, Transport properties of monolayer MoS_2 grown by chemical vapor deposition, Nano Lett. **14**, 1909 (2014).

[21] O. Lopez-Sanchez, D. Lembke, M. Kayci, A. Radenovic, and A. Kis, Ultrasensitive photodetectors based on monolayer MoS_2, Nat. Nanotechnol. **8**, 497 (2013).

[22] J.-H. Ahn, W. M. Parkin, C. H. Naylor, A. T. C. Johnson, and M. Drndić, Ambient effects on electrical characteristics of CVD-grown monolayer MoS_2 field-effect transistors, Sci. Rep. **7**, 4075 (2017).

[23] J. Lee, S. Kang, K. Yim, K. Y. Kim, H. W. Jang, Y. Kang, and S. Han, Hydrogen evolution reaction at anion vacancy of two-dimensional transition-metal dichalcogenides: Ab initio computational screening, J. Phys. Chem. Lett. **9**, 2049 (2018).

[24] X. Zhang, S. Wang, C. K. Lee, C. M. Cheng, J. C. Lan, X. Li, J. Qiao, and X. Tao, Unravelling the effect of sulfur vacancies on the electronic structure of the MoS_2 crystal, Phys. Chem. Chem. Phys. **22**, 21776 (2020).

[25] Y. Liu and F. Gu, A wafer-scale synthesis of monolayer MoS_2 and their field-effect transistors toward practical applications, Nanoscale Adv. **3**, 2117 (2021).

[26] M. R. Laskar, p-type doping of MoS_2 thin films using Nb, Appl. Phys. Lett. **104**, 092104 (2014).

[27] J. S. Lee, C. S. Park, T. Y. Kim, Y. S. Kim, and E. K. Kim, Characteristics of p-type conduction in P-doped MoS_2 by phosphorous pentoxide during chemical vapor deposition, Nanomaterials **9**, 1278 (2019).

[28] F. Zhang, B. Zheng, A. Sebastian, D. H. Olson, M. Liu, K. Fujisawa, Y. T. Hai Pham, V. O. Jimenez, V. Kalappattil, L. Miao, T. Zhang, R. Pendurthi, Y. Lei, A. L. Elías, Y. Wang, N. Alem, P. E. Hopkins, S. Das, V. H. Crespi, M.-H. Phan *et al.*, Monolayer vanadium-doped tungsten disulfide: A room-temperature dilute magnetic semiconductor, Adv. Sci. **7**, 2001174 (2020).

[29] J. Zou, Z. Cai, Y. Lai, J. Tan, R. Zhang, S. Feng, G. Wang, J. Lin, B. Liu, and H. M. Cheng, Doping concentration modulation in vanadium-doped monolayer molybdenum disulfide for synaptic transistors, ACS Nano **15**, 7340 (2021).

[30] L. A. T. Nguyen, Spin-selective hole-exciton coupling in a V-doped WSe_2 ferromagnetic semiconductor at room temperature, ACS Nano **15**, 20267 (2021).

[31] I. Williamson, S. Li, A. Correa Hernandez, M. Lawson, Y. Chen, and L. Li, Structural, electrical, phonon, and optical properties of Ti- and V-doped two-dimensional MoS_2, Chem. Phys. Lett. **674**, 157 (2017).

[32] Y. Miao, H. Bao, W. Fan, and F. Ma, Modulation of the electronic structure and magnetism performance of V-doped monolayer MoS_2 by strain engineering, J. Phys. Chem. Solids **142**, 109459 (2020).

[33] S. Mekonnen and P. Singh, Electronic structure and nearly room-temperature ferromagnetism in V-doped monolayer and bilayer MoS_2, Int. J. Mod. Phys. B **32**, 1850231 (2018).

[34] Y. Mao, Y. Fang, K. Yuan, and F. Huang, Effect of vanadium doping on the thermoelectric properties of MoS_2, J. Alloys Compd. **903**, 163921 (2022).

[35] N. Singh and U. Schwingenschlögl, A route to permanent valley polarization in monolayer MoS_2, Adv. Mater. **29**, 1600970 (2017).

[36] See Supplemental Material at http://link.aps.org/supplemental/10.1103/PhysRevMaterials.8.084002 for more detailed information regarding the schematic diagram of the growth, the time-temperature profile of the growth, the phonon-dispersion curve, optical images of the crystals, fitting of the Raman spectra, the XPS survey spectra, the temperature-, power-, and concentration-dependent PL, the atomic structure for DFT calculations, DOS, and calculations to find the value of L_D, n_{2D}, and the change in work function.

[37] S. Mignuzzi, A. J. Pollard, N. Bonini, B. Brennan, I. S. Gilmore, M. A. Pimenta, D. Richards, and D. Roy, Effect of disorder on Raman scattering of single-layer MoS_2, Phys. Rev. B **91**, 195411 (2015).

[38] K. R. Sahoo, J. J. Panda, S. Bawari, R. Sharma, D. Maity, A. Lal, R. Arenal, G. Rajalaksmi, and T. N. Narayanan, Enhanced room-temperature spin-valley coupling in V-doped MoS_2, Phys. Rev. Mater. **6**, 085202 (2022).

[39] L. Zhang, Tuning electrical conductance in bilayer MoS_2 through defect-mediated interlayer chemical bonding, ACS Nano **14**, 10265 (2020).

[40] A. Kagkoura, R. Arenal, and N. Tagmatarchis, Controlled chemical functionalization toward 3D-2D carbon nanohorn-MoS_2 heterostructures with enhanced electrocatalytic activity for protons reduction, Adv. Funct. Mater. **31**, 2105287 (2021).

[41] B. Radisavljevic and A. Kis, Mobility engineering and a metal-insulator transition in monolayer MoS_2, Nat. Mater. **12**, 815 (2013).

[42] H. Duan, P. Guo, C. Wang, H. Tan, W. Hu, W. Yan, C. Ma, L. Cai, L. Song, W. Zhang, Z. Sun, L. Wang, W. Zhao,

Y. Yin, X. Li, and S. Wei, Beating the exclusion rule against the coexistence of robust luminescence and ferromagnetism in chalcogenide monolayers, Nat. Commun. **10**, 1584 (2019).

[43] X. Zheng, A. Calò, T. Cao, X. Liu, Z. Huang, P. M. Das, M. Drndic, E. Albisetti, F. Lavini, T.-D. Li, V. Narang, W. P. King, J. W. Harrold, M. Vittadello, C. Aruta, D. Shahrjerdi, and E. Riedo, Spatial defects nanoengineering for bipolar conductivity in MoS_2, Nat. Commun. **11**, 3463 (2020).

[44] W. Bao, X. Cai, D. Kim, K. Sridhara, and M. S. Fuhrer, High mobility ambipolar MoS_2 field-effect transistors: Substrate and dielectric effects, Appl. Phys. Lett. **102**, 042104 (2013).

[45] P. D. Patil, S. Ghosh, M. Wasala, S. Lei, R. Vajtai, P. M. Ajayan, and S. Talapatra, Electric double layer field-effect transistors using two-dimensional (2D) layers of copper indium selenide ($CuIn_7se_{11}$), Electronics **8**, 645 (2019).

[46] J. Pandey and A. Soni, Unraveling biexciton and excitonic excited states from defect bound states in monolayer MoS_2, Appl. Surf. Sci. **463**, 52 (2019).

[47] S. Dubey, Weakly trapped, charged, and free excitons in single-layer MoS_2 in the presence of defects, strain, and charged impurities, ACS Nano **11**, 11206 (2017).

[48] W. Zhou, X. Zou, S. Najmaei, Z. Liu, Y. Shi, J. Kong, J. Lou, P. M. Ajayan, B. I. Yakobson, and J. C. Idrobo, Intrinsic structural defects in monolayer molybdenum disulfide, Nano Lett. **13**, 2615 (2013).

[49] Y. Zhu, Room-temperature photoluminescence mediated by sulfur vacancies in 2D molybdenum disulfide, ACS Nano **17**, 13545 (2023).

[50] W. Bennecke, Disentangling the multiorbital contributions of excitons by photoemission exciton tomography, Nat. Commun. **15**, 1804 (2024).

[51] N. Saigal and S. Ghosh, Evidence for two distinct defect related luminescence features in monolayer MoS_2, Appl. Phys. Lett. **109**, 122105 (2016).

[52] S. Feng, Z. Lin, X. Gan, R. Lv, and M. Terrones, Doping two-dimensional materials: Ultra-sensitive sensors, band gap tuning and ferromagnetic monolayers, Nanoscale Horiz. **2**, 72 (2017).

[53] L. Yang, Q. Fu, W. Wang, J. Huang, J. Huang, J. Zhang, and B. Xiang, Large-area synthesis of monolayered $MoS_{2(1-x)}Se_{2x}$ with a tunable band gap and its enhanced electrochemical catalytic activity, Nanoscale **7**, 10490 (2015).

[54] A. Singh and A. K. Singh, Origin of n-type conductivity of monolayer MoS_2, Phys. Rev. B **99**, 121201(R) (2019).

[55] H. Wang, C. Zhang, and F. Rana, Ultrafast dynamics of defect-assisted electron-hole recombination in monolayer MoS_2, Nano Lett. **15**, 339 (2015).